

# The supernova-regulated ISM - III. Magnetic fields in the multi-phase gas

C.C. Evirgen<sup>1\*</sup>, A. Shukurov<sup>1</sup>, F.A. Gent<sup>2</sup> and A. Fletcher<sup>1</sup>.

<sup>1</sup>*School of Mathematics and Statistics, Newcastle University, Newcastle upon Tyne, UK, NE1 7RU*

<sup>2</sup>*SP<sup>2</sup>RC, School of Mathematics and Statistics, University of Sheffield, Sheffield, UK, S3 7RH*

Accepted -. Received -; in original form -

## ABSTRACT

...

**Key words:** ...

## 1 INTRODUCTION

FAG – notes – include Beck, Fletcher, Berkhuijsen observations of magnetic fields (Fletcher et al. 2011) and observation/estimates of multiphase structure (Cox & Smith 1974; McKee & Ostriker 1977)

The results presented in this paper are based on simulations of the multiphase interstellar medium (ISM) reported in Gent et al. (2013a) and Gent et al. (2013b), subsequently referred to as Paper I and Paper II, respectively. In particular we consider a model, identified as B1 $\Omega$ s in Paper II. Supernova(SN)-driven turbulence is applied to ISM in a section of a spiral galaxy differentially rotating, stratified about the galactic disk and subject to, radiative cooling (Sarazin & White 1987; Wolfire et al. 1995), photoelectric heating (Wolfire et al. 1995) and other transport processes. The rate and distribution of SN explosions, gravity (Kuijken & Gilmore 1989) and angular momentum are consistent with observational parameters for the solar neighbourhood (Ferrière 2001). A nano Gauss seed magnetic field is applied and amplified by dynamo until it saturates with a mean magnetic strength of a few micro Gauss, remarkably consistent with observed estimates for the Milky Way (References? 00).

Models of the magnetized ISM (Heitsch et al. 2001; Mac Low et al. 2005) have explored the effects of magnetic field on the localized ISM, including the fluctuation dynamo, but without the effects of stratification and the large scale structure induced by the differential rotation of the disk. Large scale structure in the stratified ISM has been investigated by de Avillez & Breitschwerdt (2005), but without differential rotation the dynamo to grow the field to full strength is absent, so an imposed field is applied. Hanasz et al. (2005); Dobbs & Price (2008) and Hanasz et al. (2009) apply magnetic fields to global disk models, including a dynamo, but

due to numerical constraints must limit or exclude vertical stratification and multi-phase gas composition. Korpi et al. (1999) and Gressel et al. (2008) conducted earlier simulations with the same approach as described here, but with lower resolution and higher diffusion were unable to follow the dynamo through to saturation. The advantage of the results from Paper II is that the magnetic field produced is not imposed, but evolves dynamically under realistic physical processes governing the formation of the thermohydrodynamic structure of the ISM. From this point of view it is of great value for appreciating the multi-phase structure of the magnetized ISM and for comparison with observation.

Twelve snapshots in the time range,  $1.40 \text{ Gyr} < t < 1.67 \text{ Gyr}$  are used. This time range corresponds to the steady-state phase of the system. In addition, there are two potential SN remnants, which provide isolated structures of hot gas. In addition, a snapshot at  $t = 1.4 \text{ Gyr}$  is also presented (Figure 8) to illustrate the effect of the hot phase on the magnetic field.

The multi-phase structure is defined in terms of temperature and density. However, an equivalent definition is given in terms of entropy, which has an explicit definition linking density and temperature (Gent 2012). The cold, warm and hot phases are defined by the entropy ranges,  $s \leq 3.7 \cdot 10^8$ ,  $3.7 \cdot 10^8 < s < 23.2 \cdot 10^8$  and  $s > 23.2 \cdot 10^8 \text{ erg g}^{-1} \text{ K}^{-1}$ , respectively.

## 2 THE MEAN MAGNETIC FIELD

The decomposition of the magnetic field into mean and fluctuating (random) field follows Paper II. Volume averaging with a Gaussian kernel,  $G_l(\mathbf{x} - \mathbf{x}')$  is used to decompose the magnetic field,  $\mathbf{B}$ , into mean (large-scale),  $\mathbf{B}_l$  and random (small-scale),  $\mathbf{b}_l$ , fields. The decomposition is given by

$$\mathbf{B} = \mathbf{B}_l + \mathbf{b}_l, \quad \mathbf{B}_l = \langle \mathbf{B} \rangle_l. \quad (1)$$

\* E-mail: c.c.evirgen@newcastle.ac.uk (CCE); anvar.shukurov@newcastle.ac.uk (AS); f.gent@shef.ac.uk (FAG); andrew.fletcher@newcastle.ac.uk (AF)

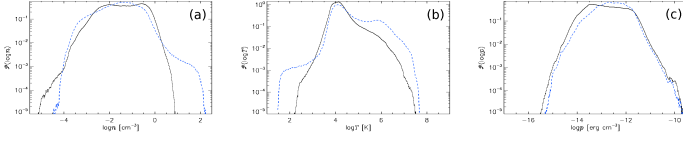


**Figure 1.** Volume weighted probability distributions of gas number density (a), temperature (b) and thermal pressure (c) for models H1Ω (black, solid) and B1Ω (blue, dashed) for the total numerical domain  $|z| \leq 1.12$  kpc.

Gaussian smoothing of the magnetic field with kernel size  $l$  is represented by

$$\langle \mathbf{B} \rangle_l = \int_V \mathbf{B}(\mathbf{x}') G_l(\mathbf{x} - \mathbf{x}') d^3 \mathbf{x}', \quad (2)$$

$$G_l(\mathbf{x}) = (2\pi l^2)^{-3/2} \exp[-\mathbf{x}/(2l^2)],$$

where  $l \approx 50$  pc is half the integral scale of random motions, as discussed in Paper I. Preliminary analysis does not show significant sensitivity of the mean or random field to variations in  $l$  within the range  $0 < l < 100$  pc. However, future work will consider analysis of isolated structures in the ISM. A more detailed analysis of length and correlation scales will be carried out. However, the current definition,  $l = 50$  pc, is sufficient for the purposes of this paper.

### 3 THREE-PHASE STRUCTURE OF THE FIELD

The total volume probability distributions for gas number density  $n$ , temperature  $T$  and thermal pressure  $p$  are displayed in Fig. 1 from Models B1Ω (black, solid) and H1Ω (blue, dashed). Note that Model H1Ω includes the correction to the SN distribution, which stabilises the disc against unphysical cyclic oscillations, although it is still subject to natural random vertical fluctuations. Hence the mean density in the SN active region remains consistently higher than in Model WSWa.

Although the three phase temperature distribution is still visible for this model in Fig. 1b, it is less pronounced than the results from Model WSWa shown in Fig. ??b. However the three phase structure for the MHD Model B1Ω is not at all apparent in panel b, with a significantly narrower range of temperatures. The bulk of the density distributions (a) are quite similar between the HD and MHD models, except that the high densities are not as well resolved in the MHD models. The thermal pressure distributions are very similar, but with the HD modal pressure approximately one third the MHD modal pressure.

The effect of the magnetic pressure in Model B1Ω is to expand the thick disc further than Model H1Ω and this is illustrated in Fig. 2a, where the horizontal averages of gas number density  $n(z)$  are plotted against  $z$  for both models. The strong peak in the density at the mid-plane is evident for Model H1Ω (black, solid), while for Model B1Ω (blue, dashed) there is a broad plateau in the density, extending to  $|z| \simeq 300$  pc, where the mean magnetic field is strongest.

The horizontal averages of the pressure are plotted in Fig. 2b for both models. There is a strong peak at the mid-plane in the turbulent pressure for the HD model (black, dashed), but a much weaker profile for the MHD model

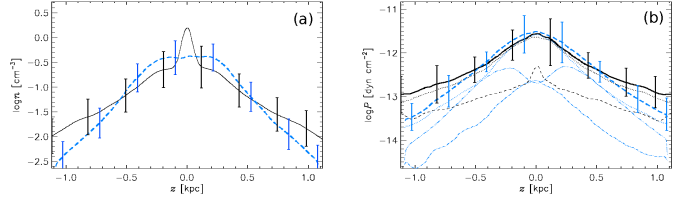


**Figure 2.** Horizontal averages of gas number density,  $\bar{n}(z)$  (a), and total pressure,  $\bar{P}(z)$  (b), for Model B1Ω (solid, black), and Model H1Ω (dashed, blue). Each are time-averaged using eleven snapshots respectively, spanning 100 Myr. The vertical lines indicate standard deviation within each horizontal slice. The thermal  $\bar{p}(z)$  (dotted) and ram  $\bar{p}_{\text{turb}}(z)$  (fine dashed) pressures are also plotted (b). For Model WSWa the magnetic pressure  $\bar{p}_B$  is also plotted (fine, dash-3dotted).

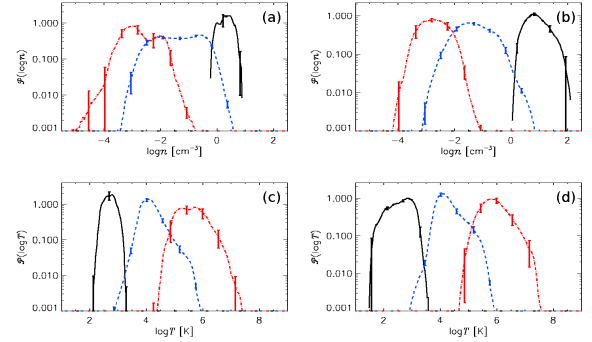


**Figure 3.** Probability distributions by phase: cold (blue, dashed), warm (black, solid) and hot (red, dash-dotted) for gas number density ( $n$  (a), (b)) and temperature ( $T$  (c), (d)) for Model B1Ω ((a), (c)) and Model H1Ω ((b), (d)). 95% confidence intervals for temporal deviation are shown as error bars.

(blue, dash-dotted). There are two peaks in the magnetic pressure (blue, dash-3dotted) near  $|z| \simeq 200$  pc, which supports the extended density profile. Another possible effect, which might constrain the circulation of the hot gas, and hence enhance the pressure at the mid-plane, is the strong horizontal orientation of the field. As mentioned in Section 7.2 in Gent (2012) the periodic boundary conditions exclude a non-zero vertical component to the mean field, so the magnetic tension predominantly acts against the vertical flows. Some understanding of the multi-phase structure of the magnetised ISM is still possible from these models, but the extreme temperatures and densities are significantly under represented. To improve this in future work it will be desirable to allow unrestricted evolution of vertical field and to apply realistic clustering of the SNe to generate more superbubbles (composite multiple SN remnants forming a single superstructure) or chimneys (plumes venting hot gas from the disc towards the halo).

Results for separation of the ISM into three phases using the method detailed in Section ?? are shown for Models B1Ω and H1Ω in Fig 3 with total volume probability distributions. The phases are defined using entropy  $s$  such that for cold  $s < 4.4 \cdot 10^8 \text{ erg g}^{-1} \text{ K}^{-1}$  and hot  $s > 23.2 \cdot 10^8 \text{ erg g}^{-1} \text{ K}^{-1}$  with warm in between. Apart from the higher densities for the cold phase with the HD model (panel b), anticipated by the volume distributions (Fig. 1),

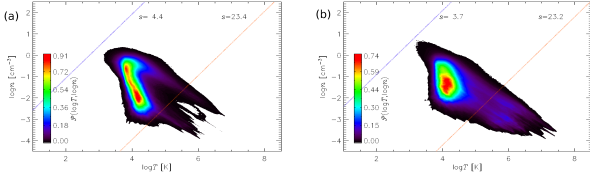


**Figure 4.** Probability contour plot by volume of  $\log n$  vs  $\log T$  for Model B1 $\Omega$  (a) and Model H1 $\Omega$  (b). The lines of constant entropy  $s = 4.4 \cdot 10^8$  and  $23.2 \cdot 10^8 \text{ erg g}^{-1} \text{ K}^{-1}$  indicate where the phases are defined as cold for  $s \leq 4.4$  and as hot for  $s > 23.2$ .

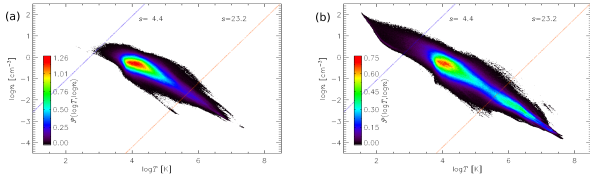


**Figure 5.** The mid-plane probability distributions ( $|z| < 100 \text{ pc}$ ) by gas number density  $\log n$  and temperature  $\log T$  for (a) Model B1 $\Omega$  and (b) Model H1 $\Omega$ .

the warm and hot distributions for the MHD density (panel a) are broad, with a bimodal structure to the hot gas. The distributions for the warm gas (panels c and d) are very similar and for the cold (hot) distributions the MHD model does not extend to as low (high) temperatures.

Comparing the combined probability distribution of density and temperature for both of these models in Fig. 4 with those of Model WSWa in Fig. ?? the spread is more broad and not obviously aligned along a line of constant pressure. The HD distribution here is less compact than with MHD. However when considering only the mid-plane distributions, as displayed in Fig. 5 the distributions match better with Model WSWa and the pressure alignment is evident. So the broad distributions for the total volumes are explained by the stronger gradient in the pressure distribution, due to the reduced stirring of the hot gas. The thermal pressure at the mid-plane is also very similar in both models, reflected also in the agreement of the total and thermal pressure near the mid-plane in the plot of horizontal averages (Fig 2b). The magnetic and turbulent pressure in Model B1 $\Omega$  combine to match the mid-plane turbulent pressure alone of Model H1 $\Omega$ . For the temperature in Model B1 $\Omega$  the hot gas has two modes, evident in Fig. 4a at  $10^5 \text{ K}$  and  $10^6 \text{ K}$ , but at the mid-plane there only the single  $10^3 \text{ K}$  mode. The structure of the ISM at the mid-plane is therefore common to both models with modes at  $10^6 \text{ K}$ ,  $10^{-2} \text{ cm}^{-3}$  and  $10^4 \text{ K}$ ,  $1 \text{ cm}^{-3}$ . The cold gas is insufficiently resolved in Model B1 $\Omega$  for comparison.

There is no evident dependence in the probability distributions between the MHD models differing in rotation, shear or SN rate. The models in the kinematic stage extend to lower densities and higher temperatures than either the HD Model H1 $\Omega$  or the MHD models in the dynamo saturated state, and also extend to lower pressures.

In Fig. 6a the joint probability distributions of gas number density with magnetic field strength is shown and in Fig. 6b of temperature with magnetic field strength for

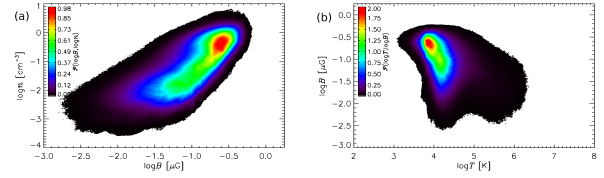


**Figure 6.** Total volume probability distributions ( $|z| < 100 \text{ pc}$ ) by gas number density  $\log n$  and magnetic field strength  $\log |B|$  (a) and temperature  $\log |T|$  and magnetic field strength  $\log |B|$  (b) for Model B1 $\Omega$ .

Model B1 $\Omega$ . From (a) it is clear there is a strong positive correlation between magnetic field strength and density and from (b) a weak negative correlation between temperature and field strength. The  $T, B$  distribution has very strong peak at  $T = 10^4 \text{ K}$ .

For Model B1 $\Omega$  the ISM for a single snapshot is decomposed into the three phases and the magnetic field for each plotted separately in Fig. 7. In panel a the cold gas occupies only a limited volume near the mid-plane, but the magnetic field is very strong and organised in alignment with the mean field surrounding it in the warm gas. This is represented by the length and thickness of the vector arrows. The colour of the arrows emphasises that the alignment has a strong azimuthal component. No arrows are present away from the mid-plane, because the cold gas is absent there. In panel b the warm gas is present throughout the numerical volume. Field vectors are present almost throughout and the field is highly aligned, mainly in the azimuthal direction. The strength of the field increases towards the mid-plane. The presence of some vectors in blue or grey indicates that there are significant perturbations where the field includes reversals, some of these strong. Some of the field exhibits significant vertical orientation, but it is mainly horizontal. In panel (c) the hot gas is also present throughout the volume, although in smaller amounts near the mid-plane. Despite this there is very little magnetic field. What field there is generally weak and lacks much systematic alignment, although any orientation tends to be vertical, consistent with the field lines being stretched by the gas flowing away from the mid-plane. Effectively the hot gas has a very weak field, which is highly disordered. Most of the magnetic field, and particularly the mean field, occupies the warm gas. Detailed quantitative analysis of the structure of the gas will be deferred to future work.

### 3.1 Summary

The magnitude of the magnetic field is strongly aligned to the density of the ISM and indirectly the warm and cold phases. More particularly the mean field is stronger in the warm and cold gas, with the hot gas containing a more random field. The mean magnetic field and the magnetic energy is strongest at  $|z| \simeq 300 \text{ pc}$ , just outside the SNe active region. The fluctuating dynamo is likely to be strongest in this SNe active region, but due to the low magnetic Reynolds numbers in the simulations, it is likely that the field and energy is significantly weaker in the simulations than might be expected.

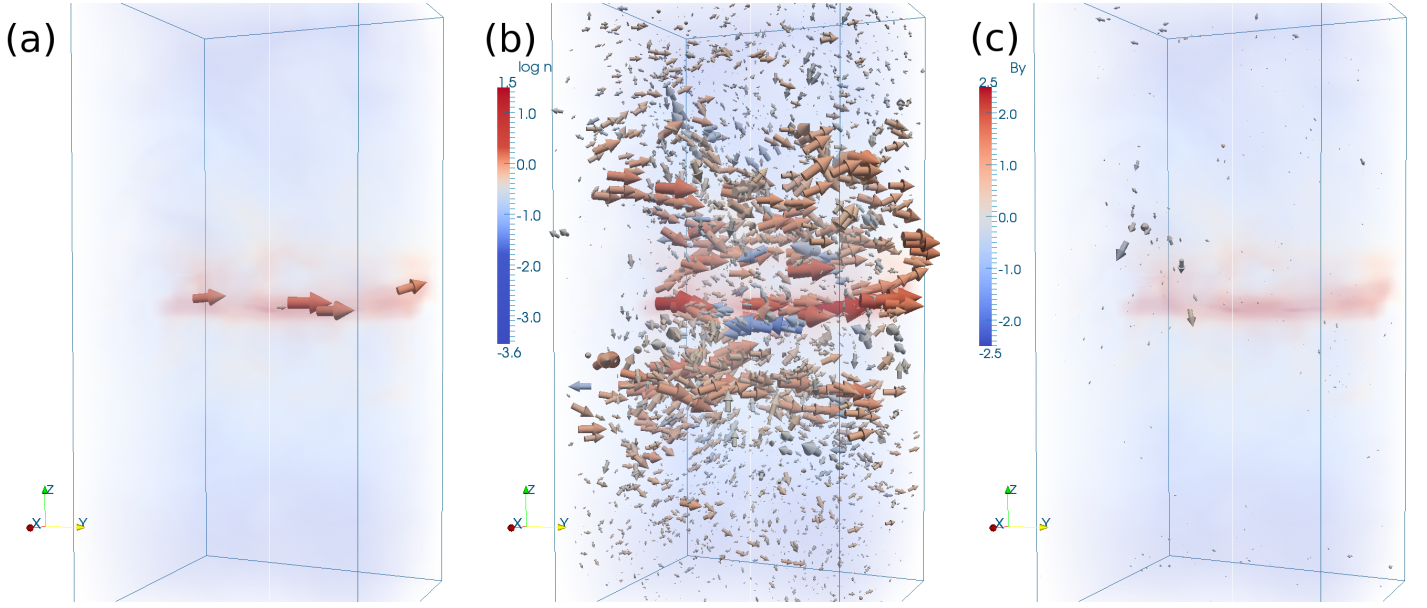


**Figure 7.** Vector plots of the magnetic field  $\mathbf{B}$  (a) in the cold phase (b) the warm phase and (c) the hot phase. Field directions are indicated by arrows and strength by their thickness. The colour of the arrows indicates the strength of the azimuthal ( $y$ ) component (colour bar on the right). The background shading illustrates the density of the ISM.

#### 4 MAGNETIC FIELD LINES

Magnetic field lines give a qualitative description of the magnetic field in the ISM. We introduce sampling of physical variables along the field lines of the magnetic field, to obtain a quantitative description of the observables. Observables, such as entropy or pulsar RM measures (Stepanov et al. 2002) are frequently used to derive other observables or statistics. The use of sampling along field lines will enable the analysis of observables across many snapshots, whilst avoiding the use of time averages, which is not sensible for observables associated to a turbulent flow (Tennekes & Lumley 1972). For example, wavelet transform methods are used by Stepanov et al. (2002), to derive the Galactic magnetic field from pulsar RM data. Field lines of the Galactic magnetic field can be derived from this analysis and it can be further analysed using sampling along the field lines.

The mean magnetic field is considered first, to explore the large-scale characteristics of the magnetic field, having extracted the random, small-scale fluctuations with Gaussian volume averaging. Intuition suggests that the mean magnetic field will prefer to stay in the warm phase, which provides a less hostile environment for the magnetic field than the transonic, compressible turbulence of the hot phase. This will be discussed using the field lines and by comparison with a test case.

##### 4.1 Field line equation for a vector field, $\mathbf{B}(\mathbf{x})$

Given a vector field,  $\mathbf{B}(\mathbf{x})$ , in Cartesian coordinates, its field lines are described by

$$\frac{dx}{B_x} = \frac{dy}{B_y} = \frac{dz}{B_z} = ds, \quad (3)$$

where  $ds$  is a separation constant used to integrate along the field line. This is formulated as

$$\begin{cases} \frac{dx}{ds} = B_x, \\ \frac{dy}{ds} = B_y, \\ \frac{dz}{ds} = B_z, \end{cases} \quad (4)$$

The field line equation is integrated along  $x$ ,  $y$  and  $z$  to obtain the field lines,

$$L : (x(s), y(s), z(s)),$$

which are integrated using a 4<sup>th</sup>-order Runge-Kutta scheme. For discrete-valued  $\mathbf{B}(\mathbf{x})$  interpolation is used to evaluate its components at positions,  $\mathbf{x}$ , which do not lie on the data grid.

##### 4.1.1 Sampling observables along field lines

Having obtained a set of field lines, observables are sampled on each point along the field lines. The multi-phase structure of the ISM gas and the turbulent flows within the ISM gas suggest that the data obtained from sampling these observables along the field lines will not necessarily have a simple, parametric statistical description. Consequently, the use of histograms to represent the data could be misleading where the convergence of the histograms pose a non-trivial problem. We circumvent this issue by using Gaussian kernel density estimation, which provides a non-parametric method for obtaining a probability density function (PDF) of the sampled observable data. Preliminary work included observables such as density and temperature. However, we have found that PDFs of entropy provide sufficient information. Thus, we restrict our attention to PDFs of specific entropy,  $s$ , sampled along field lines. This PDF is expressed as  $\mathcal{P}(s)$ . The definition of the multi-phase structure is given

below in terms of specific entropy,  $s$ , with units  $\text{erg g}^{-1} \text{K}^{-1}$ :

$$\begin{cases} \text{Cold phase:} & s \leq 3.7 \cdot 10^8, \\ \text{Warm phase:} & 3.7 \cdot 10^8 < s \leq 23.2 \cdot 10^8, \\ \text{Hot phase:} & s > 23.2 \cdot 10^8. \end{cases} \quad (5)$$

We define the probability of finding a point along a field line in each of the phases using the phase definitions. These are

$$\begin{aligned} \mathcal{P}(\text{cold phase}) &\equiv \mathcal{P}(s \leq 3.7 \cdot 10^8), \\ \mathcal{P}(\text{warm phase}) &\equiv \mathcal{P}(3.7 \cdot 10^8 < s < 23.2 \cdot 10^8), \\ \mathcal{P}(\text{hot phase}) &\equiv \mathcal{P}(s > 23.2 \cdot 10^8). \end{aligned} \quad (6)$$

We make extensive use of PDFs of sampled variables, both graphically and to make specific statements about the characteristics of the magnetic fields in the ISM.

#### 4.1.2 Analysis of the sensitivity of magnetic field lines to the multi-phase structure

Even though the visualisation is informative, it is necessary to determine whether the field lines are sensitive to the phases of the ISM. Consequently, we compare the characteristics of the field lines against straight lines launched in the azimuthal ( $y$ ) direction, from the seed points used to compute the field lines. This test is devised using ideas from the field of stereology (Baddeley & Jensen 2004), lineal analysis in particular. The straight lines used in the test case will have the same general characteristics as the field lines, since they both traverse the computational domain in the positive  $y$ -direction. This ensures that the lines are representative of the field lines being sampled. Despite having the same general characteristics, the straight lines should not be sensitive to the phases of the ISM; they will not prefer to stay in a particular phase, whilst avoiding others. Therefore, comparison of the PDFs of the observables sampled along the field lines and the straight lines, should identify sensitivity (or lack thereof) of the field lines to the phases of the ISM.

In addition, similar samples can be taken from snapshots which are statistically independent in time. If the seeding for the field line calculations are carried out identically for each snapshot, a physically meaningful ensemble average is obtained. The twelve snapshots used in this paper are statistically independent in time and are taken from the statistically-steady phase of the system.

#### 4.1.3 Correlation analysis of magnetic field lines using PDFs

We also use PDFs to analyse the correlation lengths of the magnetic fields in the multi-phase. We calculate the maximum displacement of the field lines from their seed point,  $r$ , and their maximum displacement along the  $x$ ,  $y$  and  $z$  axes,  $r_x$ ,  $r_y$  and  $r_z$ , respectively. PDFs of these quantities are calculated using kernel density estimation. As an example, we consider some field line,  $L_i$ , with seed point,  $\mathbf{x}_0 \equiv (x_0, y_0, z_0)$ . The field line must have a minimum and maximum displacement from the seed point, which is a direct consequence of the solenoidality of the magnetic field. The maximum displacement occurs at some  $\mathbf{x}_{max}$  along  $L_i$  such that  $r = |\mathbf{x}_{max} - \mathbf{x}|$ . The maximum displacements along the axes are described by  $r_x = x_{max} - x_0$ ,

$r_y = y_{max} - y_0$ ,  $r_z = z_{max} - z_0$ . We calculate typical length scales for each of these displacements, using the mean of the random variable. For example, for  $r$ , we use

$$C = \int_{r_{min}}^{r_{max}} r \mathcal{P}(r) dr, \quad (7)$$

where  $r_{min}$  and  $r_{max}$  are the minimum and maximum values of  $r$  observed across all snapshots and  $\mathcal{P}(r)$  is the PDF of  $r$ . The typical length scales  $C_x$ ,  $C_y$ ,  $C_z$  along the  $x$ ,  $y$  and  $z$  axes, respectively, are calculated using similar expressions.

## 4.2 The phase that hosts the magnetic field

The mean magnetic field is considered first, to explore the large-scale characteristics of the magnetic field, having extracted the small-scale fluctuations with Gaussian volume averaging. Intuition suggests that the mean magnetic field will prefer to stay in the warm phase, which provides a less hostile environment for the magnetic field than the transonic, compressible turbulence of the hot phase. As discussed in Section , the magnetic field is very strong and well-aligned with the azimuthal ( $y$ ) direction in the  $|z| < 0.6 \text{ kpc}$  region, where the warm phase dominates. In the  $0.6 < |z| < 1.0 \text{ kpc}$  region, the hot phase dominates. Consequently, the magnetic field is not well aligned and much weaker than the magnetic field in the warm phase. The turbulent flows in the  $0.6 < |z| < 1.0 \text{ kpc}$  region will have the highest kinetic energies throughout the ISM (CALCULATE THESE AVERAGE VALUES). Conversely, the magnetic field is very weak in the hot phase (Fig. 6). Subsequently, the kinetic energy of the flows should be at least of a comparable order to the magnetic field energy in this region. We expect this to cause distortions in the magnetic field (CCE: REFERENCE TAYLOR HERE). The lack of alignment and weakness of the magnetic field in this region (Fig. 7) imply that the magnetic field is sensitive to the hot phase. The characteristics of the magnetic field lines further clarify the effect of the hot phase on the magnetic field.

#### 4.2.1 Distortion of the mean magnetic field lines in the hot phase

In Figure 8, data from the snapshot at  $t = 1.4 \text{ Gyr}$  are used. The white field lines have been seeded along the  $xz$ -axis at  $y = -0.51 \text{ kpc}$ . The translucent gas inside the box is a representation of the log density field. Density decreases from brighter to darker colours. Since the warm and hot phase represents approximately 99% of the fractional volume of the ISM gas, it is only useful for visualising the characteristics of the field line within the warm and hot phases. We will present a preliminary result regarding the field lines within the cold phase in this paper. However, a more detailed discussion will be reported elsewhere. For descriptive purposes, the yellow shades of gas correspond to warm gas and the red shades correspond to the hot phase. We note that the field lines are generally aligned with the positive  $y$ -direction, especially in the warm phase and the field lines are smooth inside the warm gas. However, we notice significant differences in the characteristics of the field lines in the hot phase.

There is an isolated structure of hot gas (likely to be a SN remnant) in the (approximate) range  $-0.8 < z < -1.1 \text{ kpc}$ . The field lines in this region still traverse the



computational domain in the positive  $y$ -direction. However, they are distorted and stretched in the positive  $z$ -direction in the region surrounding the hot gas.

Similarly, in the range  $0.7 < z < 1.1$  kpc, there is a larger structure of hot gas, which spans the  $xy$ -plane. This structure appears to be part of rising hot gas, which is leaving the computational domain. As it leaves, it elongates the magnetic field lines until they are no longer connected inside the domain. Consequently, the field lines are approximately perpendicular to the  $y$ -axis, where the magnetic field lines are stretched and distorted by the hot phase. Figure 9 shows the probability density functions (PDFs) of entropy sampled along field lines (solid lines) and straight lines (dashed lines) for the snapshot at  $t = 1.4$  Gyr. The PDFs show that the magnetic field lines and straight lines have similar overall behaviour, due to their alignment in the  $y$ -direction. The alignment of the straight lines in the azimuthal ( $y$ ) direction was chosen to ensure that the straight lines are representative of the general alignment of the magnetic field, without introducing any sensitivity to the multi-phase structure.

We now consider the PDFs entropy along the field lines and straight lines in Figure 9. Firstly, we observe similar peaks in the warm phase. This agrees with Figure 8 in that the field lines are not sensitive to the warm phase. The probabilities of traversing the phases, for the field lines and straight lines, are given in Table 2. We observe that the probabilities of the straight lines traversing each phase closely match the fractional volumes of the phases, as expected; lines that are not phase-sensitive should traverse each phase with probability proportional to the fractional volume.

On the other hand, the probability of a field line traversing the hot phase is significantly higher than that of a straight line, which reiterates the effect of the stretching of field lines by the phase. The probability of a field line traversing the warm phase is lower than that of a straight line. However, this is a direct consequence of the distortion of the magnetic field by the hot phase. The probability of the field line crossing the cold phase is much smaller than 1% for both field lines and straight lines. The fractional volume of the cold phase is typically very small. Consequently, a different approach is required to analyse the characteristics of the magnetic field in the cold phase.

Overall, the magnetic field lines traverse the ISM in the azimuthal direction. This trend is observed clearly in the warm phase, where the magnetic field is not distorted by the flows of the ISM gas. Since the field lines represent lines of magnetic flux density, the distortion of the magnetic field lines by the hot phase explains the weakness of the magnetic field observed in the hot phase. The stretching of the magnetic field lines effectively wrap the field lines around the hot gas, which increases the field line density on the boundary of the hot and warm gas. Consequently, field lines do not pass through the hot gas (Fig. 8) and we observe that the magnetic field in the hot phase is very weak and lacking alignment. This strongly suggests that the magnetic field resides in the warm phase.

### 4.3 The mean and random magnetic fields

We use Equation (3) to construct field lines for the random magnetic field using the same method as for field lines of

Probability	Mean field lines	Straight lines
$\mathcal{P}(\text{cold phase})$	$\ll 0.01$	$\ll 0.01$
$\mathcal{P}(\text{warm phase})$	0.79	0.89
$\mathcal{P}(\text{hot phase})$	0.20	0.11

Table 1: Respective probabilities of finding the field and straight in the cold, warm and hot phases.

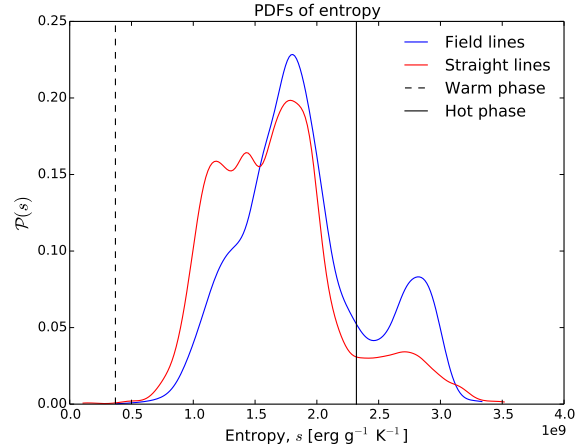


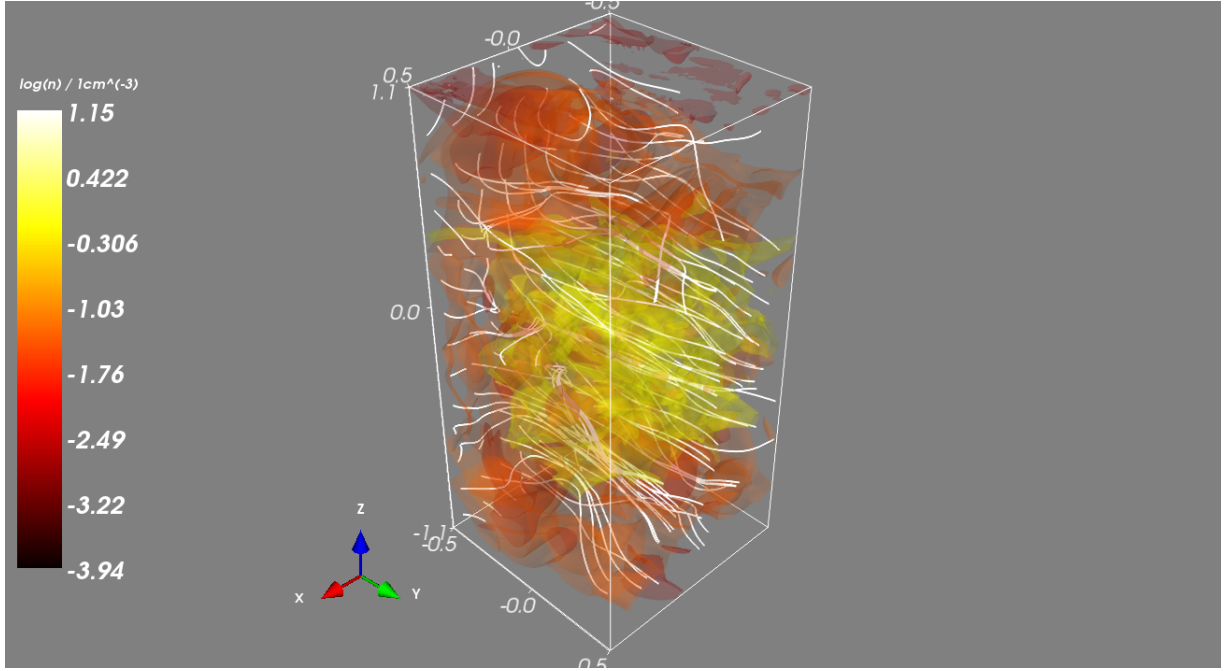
Figure 9. PDFs of entropy sampled along field lines (blue) and straight lines (red).

the mean magnetic field. Sampling along these lines (across twelve snapshots) is used to obtain the PDF of entropy, as seen in the previous section for the mean magnetic field.

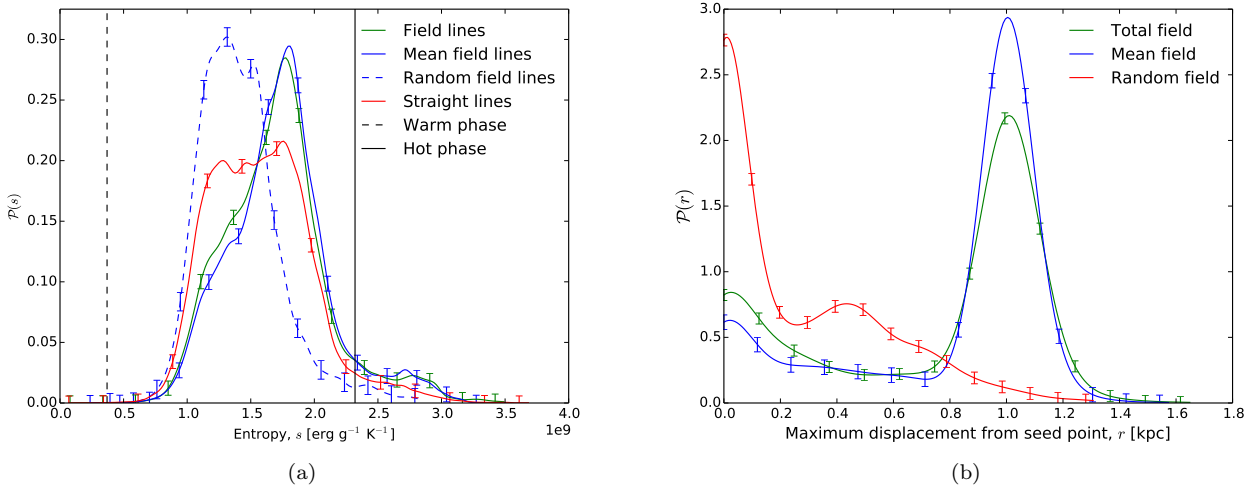
#### 4.3.1 Ensemble averaged characteristics of the mean and random magnetic field lines

Fig. 10 shows the PDF of entropy sampled along the mean field (blue solid). We note that the probability density in the cold phase is still negligible, despite larger data set used. In the warm phase, the PDF peaks at a similar value to that of entropy in Fig. 9. However, we do not observe a sharp peak for entropy of the mean field in the hot phase in Fig. 10. Nonetheless, the probability density of entropy in the hot phase is consistently higher than the PDF of entropy for straight lines. The difference can be attributed to the significant stretching of the mean magnetic field in the hot phase in the snapshot at  $t = 1.4$  Gyr and the larger data set used for the ensemble average. Stretching of the mean field occurs in other snapshots, albeit to a less severe extent. Severe stretching of the magnetic field occurs where a SN remnant is present. As discussed in the previous section, the field lines of the mean magnetic field has a greater probability density in the hot phase than the straight lines, which indicates that the stretching of the field lines by hot gas is a general characteristic. The PDF of entropy sampled along mean magnetic field lines is also more skewed towards higher entropies in the warm phase than the PDF of entropy sampled along straight lines, which suggests the mean magnetic field prefers to stay in hot, low density regions of the warm phase.

In contrast, we observe that the PDF of entropy sampled



**Figure 8.** 3D rendering of the field lines of the mean magnetic field at  $t = 1.4$  Gyr. The white lines are field lines seeded along a regular grid on the  $xz$ -plane at  $y = -0.51$  kpc.



**Figure 10.** (a) PDFs of  $s$  along field lines of the mean (blue solid), total (red solid) and random (green solid) magnetic fields. The boundaries of between the cold and warm phases (black dashed) and between the warm and hot phases (black solid) are indicated. (b) PDFs of maximum distance from the seed point of field lines for the mean (blue solid), total (green solid) and random (red solid) magnetic fields.

along the random magnetic field lines is skewed towards cooler, denser regions of the warm phase. Further, the probability density of the PDF for the random field is consistently lower than that of the straight lines, in the hot phase. This is unexpected given the random (generally unaligned and weak) nature of the magnetic field in the hot phase. This agrees with preliminary work carried out on 3D vector plots of the random magnetic field. We observed that the random magnetic field is weak in pockets of hot gas. The PDF of the mean field and the random field are visibly different

(and also by the two-sample Kolmogorov-Smirnov test). The PDF of the total field is similar to that of the mean field, as expected; the mean field contains the large-scale characteristic of the total field. However, we notice that the PDF of the total field is skewed to the left of the PDF of the mean field, in the warm phase, despite its similar shape. This is a direct effect of the random field within the total field. We see further evidence of this in the hot phase. Even though the PDFs of the mean and the total field are similar, the

local maxima of the PDF of the mean field is not observed in the PDF of the total field, in the hot phase.

Figure 10 on the preceding page shows these PDFs. Firstly, we note that all of the PDFs are clustered in the warm and hot phases. However, this is inextricably linked to the fractional volumes of the phases. It is difficult to discuss whether avoidance of the cold phase by the field line is also a contributing factor.

We concentrate on the warm and hot phases. The PDF for the total field is similar to that of the mean field in the warm phase. They both have a smooth distribution, even though the PDF of the total appears to be slightly more skewed. In the hot phase, the PDF for the total field is smooth. However, the PDF of the mean field peaks sharply, at approximately  $s = 27 \cdot 10^8 \text{ erg g}^{-1} \text{ K}^{-1}$ . Even though the PDF for the total field is smooth, its local maxima is close to this value of  $s$ . A similarly sharp peak is observed in this region for the PDF of the random field. This could suggest that  $s = 27 \cdot 10^8 \text{ erg g}^{-1} \text{ K}^{-1}$  is a characteristic entropy associated with the hot phase for this snapshot.

A sharp peak is also observed in the warm phase in the PDF for the random field, at approximately  $s = 15.5 \cdot 10^8 \text{ erg g}^{-1} \text{ K}^{-1}$ . The probability density for the random field is weak outside of the sharp regions. It appears that the random field is characterised by a small range of entropy values in the warm and hot phases.

the length scales and the velocities of the turbulence are typically higher in the hot gas than in the warm. Nevertheless, a higher resolution run would be helpful in assessing how robust is the alignment of the mean field to the warm phase, and whether the fluctuating field in the hot phase may yet have relatively greater amplitude than obtained here. Given the dominance of the dynamo about the midplane, this may be feasible without extending the domain vertically.

#### 4.4 Curve fitting for PDFs of entropy

#### 4.5 Correlation lengths of the magnetic fields

Correlation length	Total magnetic field	Mean magnetic field	Random magnetic field
$C$	0.711	0.700	0.241
$C_x$	0.061	0.045	0.065
$C_y$	0.380	0.376	0.090
$C_z$	0.124	0.084	0.105

Table 2: Correlation lengths for the total, mean and random magnetic field in kpc.

## 5 CONCLUSIONS

Note, that the mean magnetic field is strongest in the warm phase and the dynamo is strongest in the SN dense region within 500 pc of the midplane. These results support the hypothesis that the mean field is closely aligned to the warm phase of the ISM. The fluctuating magnetic field is present in similar magnitude in all phases. Note, in the warm phase, away from the midplane the magnetic field has a stronger vertical component, even though in these models the periodic boundary conditions constrain the net  $B_z$  to be zero on each horizontal slice. Given more open horizontal boundaries, we could anticipate the mean field actually to exhibit more vertical structure. With higher numerical diffusion required for the hot gas, the fluctuation dynamo in this phase may have been relatively suppressed, although the Reynolds numbers may have been higher than in the warm gas as both



## ACKNOWLEDGEMENTS

## REFERENCES

- Baddeley A., Jensen E., 2004, *Stereology for Statisticians*. Chapman & Hall/CRC Monographs on Statistics & Applied Probability, Taylor & Francis
- Cox D. P., Smith B. W., 1974, *ApJ*, 189, L105
- de Avillez M. A., Breitschwerdt D., 2005, *A&A*, 436, 585
- Dobbs C. L., Price D. J., 2008, *MNRAS*, 383, 497
- Ferrière K. M., 2001, *Rev. Mod. Phys.*, 73, 1031
- Fletcher A., Beck R., Shukurov A., Berkhuijsen E. M., Horellou C., 2011, *Monthly Notices of the Royal Astronomical Society*, 412, 2396
- Gent F. A., 2012, PhD thesis, Newcastle University School of Mathematics and Statistics
- Gent F. A., Shukurov A., Sarson A., Fletcher G. R., Mantere M. J., 2013a, *MNRAS*, 432, 1396
- Gent F. A., Shukurov A., Sarson G. R., Fletcher A., Mantere M. J., 2013b, *MNRAS*, 430, L40
- Gressel O., Elstner D., Ziegler U., Rüdiger G., 2008, *A&A*, 486, L35
- Hanasz M., Lesch H., Otimianowska-Mazur K., Kowal G., 2005, in Chyży K., Otmianowska-Mazur K., Soida M., Dettmar R.-J., eds, *The Magnetized Plasma in Galaxy Evolution Cosmic-ray-driven dynamo in galactic discs*. Jagiellonian University, Kraków, pp 162–170
- Hanasz M., Wóltański D., Kowalik K., 2009, *ApJ*, 706, L155
- Heitsch F., Mac Low M.-M., Klessen R. S., 2001, *ApJ*, 547, 280
- Korpi M. J., Brandenburg A., Shukurov A., Tuominen I., 1999, *A&A*, 350, 230
- Kuijken K., Gilmore G., 1989, *MNRAS*, 239, 605
- Mac Low M.-M., Balsara D. S., Kim J., de Avillez M. A., 2005, *ApJ*, 626, 864
- McKee C. F., Ostriker J. P., 1977, *ApJ*, 218, 148
- References? A., 00, a journal, 1, 1
- Sarazin C. L., White III R. E., 1987, *ApJ*, 320, 32
- Stepanov R., Frick P., Shukurov A., Sokoloff D., 2002, *A&A*, 391, 361
- Tennekes H., Lumley J. L., 1972, *First Course in Turbulence*. Cambridge: MIT Press
- Wolfire M. G., Hollenbach D., McKee C. F., Tielens A. G. G. M., Bakes E. L. O., 1995, *ApJ*, 443, 152